Available online at www.sciencedirect.com
ScienceDirect
Solar Energy 81 (2007) 548–564
SOLAR ENERGY
www.elsevier.com/locate/solener

Monitoring and remote failure detection of grid-connected PV systems based on satellite observations

A. Drews [a,*,1], A.C. de Keizer [b], H.G. Beyer [c,1], E. Lorenz [a,1], J. Betcke [a,1], W.G.J.H.M. van Sark [b,1], W. Heydenreich [d,1], E. Wiemken [d,1], S. Stettler [e], P. Toggweiler [e], S. Bofinger [f,1], M. Schneider [f,1], G. Heilscher [f,1], D. Heinemann [a,1]

[a] *Oldenburg University, Institute of Physics, Carl-von-Ossietzky-Str. 9-11, 26129 Oldenburg, Germany*
[b] *University of Utrecht, Copernicus Institute, Department of Science, Technology, and Society, Heidelberglaan 2, 3584 CH Utrecht, The Netherlands*
[c] *University of Applied Sciences Magdeburg-Stendal (FH), Institute of Electrical Engineering, Breitscheidstr. 2, 39114 Magdeburg, Germany*
[d] *Fraunhofer Institute for Solar Energy Systems, Heidenhofstr. 2, 79110 Freiburg, Germany*
[e] *Enecolo AG, Lindhofstr. 52, 8617 Moenchaltorf, Switzerland*
[f] *Meteocontrol GmbH, Spicherer Straße 48, 86157 Augsburg, Germany*

Received 22 March 2006; accepted 27 June 2006
Available online 28 September 2006

Communicated by: Associate Editor Arturo Morales-Acevedo

Abstract

Small grid-connected photovoltaic systems up to 5 kW_p are often not monitored because advanced surveillance systems are not economical. Hence, some system failures which lead to partial energy losses stay unnoticed for a long time. Even a failure that results in a larger energy deficit can be difficult to detect by PV laymen due to the fluctuating energy yields.

Within the EU project PVSAT-2, a fully automated performance check has been developed to assure maximum energy yields and to optimize system maintenance for small grid-connected PV systems. The aim is the early detection of system malfunctions and changing operating conditions to prevent energy and subsequent financial losses for the operator. The developed procedure is based on satellite-derived solar irradiance information that replaces on-site measurements. In conjunction with a simulation model the expected energy yield of a PV system is calculated. In case of the occurrence of a defined difference between the simulated and actual energy yield, an automated failure detection routine searches for the most probable failure sources and notifies the operator.

This paper describes the individual components of the developed procedure—the satellite-derived irradiance, the used PV simulation model, and the principles of the automated failure detection routine. Moreover, it presents results of an 8-months test phase with 100 PV systems in three European countries.

Keywords: Performance check; Satellite-derived irradiance; Automatic failure detection

1. Introduction

The number of grid-connected photovoltaic (PV) systems operating in Europe has increased enormously in the last years. About 403 MW_p has been newly installed (~360 MW_p in Germany) in 2004 (EurObserv'ER, 2005). Most of these systems range in power rating between 1 and 10 kW_p. Regular performance checks on the functioning of grid-connected systems are necessary for a reliable use and successful integration of PV into the daily energy supply. System surveillance for larger systems is usually performed by using additional hardware such as radiation sensors (pyranometers or reference cells), data loggers, or other intelligent monitoring devices. This can be expensive

* Corresponding author. Tel.: +49 441 798 3929; fax: +49 441 798 3326.
E-mail address: anja.drews@uni-oldenburg.de (A. Drews).
[1] ISES member.

0038-092X/$ - see front matter © 2006 Elsevier Ltd. All rights reserved.
doi:10.1016/j.solener.2006.06.019

Nomenclature

G	global irradiance on the horizontal plane (W/m^2)	α	temperature coefficient (°C)
D	diffuse irradiance on the horizontal plane (W/m^2)	a_1, a_2, a_3	device specific parameters
G_t	global irradiance on the tilted plane (W/m^2)	c	coefficient for different kinds of PV system assembly
d	diffuse fraction (W/m^2)	h	hour
P_{AC}	PV power output (W or kW)	t	time
ΔG, Δd, ΔG_t, ΔP_{AC}	expression of uncertainty for the named quantities (W/m^2, W)	P_{sim}	simulated PV power output (W or kW)
η_{MPP}	efficiency at maximum power point	P_{mon}	monitored PV power output (W or kW)
T_M	module temperature (°C)	P_{inst}	installed PV power output (W or kW)
T_A	ambient temperature (°C)	P^*	specially weighted and sampled power output
		P_x	power output at one point in time

and requires intensive maintenance that is only economical for larger systems. Therefore, small grid-connected PV systems up to 5 kW_p are often not checked on a regular basis. Furthermore, due to the fluctuating yield of a system resulting from the intermittent character of solar irradiance, partial system faults or decreasing performance are difficult to recognize for most operators of small systems as they usually are not PV specialists. Small as well as larger system failures that lead to partial energy loss can remain unnoticed for a long time. Besides the ecological benefits in reducing CO_2 emissions, the economic perspective for these small systems is of importance. An easy and safe-to-handle long-term service to check system performance is needed to prevent from the loss of energy for the operator, and, especially in case of granted feed-in tariffs, from severe financial losses. The feed-in tariffs in Germany, 0.406 €/kWh up to 0.568 €/kWh depending on the system type and installation (EEG, 2004), or in Spain, 0.4 €/kWh for systems smaller than 100 kW (RD, 2004), provide profits to operators and the PV industry. To secure these economical profits for small systems, cost-effective methods that detect system failures as quickly as possible are of paramount importance to increase the operating efficiency of a PV system.

Within the PVSAT-2 project such a low-cost and reliable performance check on a daily basis has been developed. The expected energy yield of a PV system is determined using irradiance data derived from the meteorological satellite Meteosat-8 replacing on-site measurements with a reference cell or a pyranometer. Required hardware, directly connected to the PV system, is reduced to a low-priced hardware device which combines a data logger and a modem in one. It records the actual energy yields at pre-defined time intervals and sends these data automatically to a central server where an automated data analysis is carried out. Moreover, the PVSAT-2 scheme provides a fully automated failure detection routine which evaluates the expected and actual energy yield in order to detect the occurrence of a malfunction and to identify the most likely failure source. The operator of a system is automatically informed and has fast Internet access to the performance data of the PV system. The strength of the developed scheme lies in the inexpensive use of satellite data that avoids costly and error-prone on-site measurements. Furthermore, surveillance algorithms provide a fast overview on the performance of a system and possible faults by automatic notification.

In this paper, the entire PVSAT-2 procedure is described. Furthermore, results from tests with historical data and an 8-months field test in Germany, The Netherlands, and Switzerland with 100 systems of voluntarily participating test users are presented. It shows the applicability in a real environment and the readiness for marketing of the developed PVSAT-2 routine. Practical experiences, benefits, as well as limitations are discussed.

2. PVSAT-2 procedure

The PVSAT-2 procedure is illustrated in its basic structure in Fig. 1. The solar irradiance is derived on an hourly basis from the data of the meteorological satellite Meteosat-8 by applying an enhanced version of the Heliosat method (Hammer, 2000; Hammer et al., 2003; Lorenz, 2004). Based only on satellite-derived irradiance data, the expected yield of a PV system is calculated using a PV simulation model as described in (Beyer et al., 2004). For the calculation of the PV system's energy yield, simulation specific technical information about the system is needed which is to be supplied once by the operator of the system. This comprises information on the major system components, manufacturer, type and number of modules, inverter as well as their technical data. Other required information are the geographic location, a description on the system's assembly (e.g., roof-integrated or free-standing), orientation, inclination, and configuration (e.g., how many substrings) (Section 3.2).

The actual energy yield of a PV system is recorded for every hour by a data logger that transmits these data every night via a telephone line to a central server. There, the achieved energy yield and the simulated values are

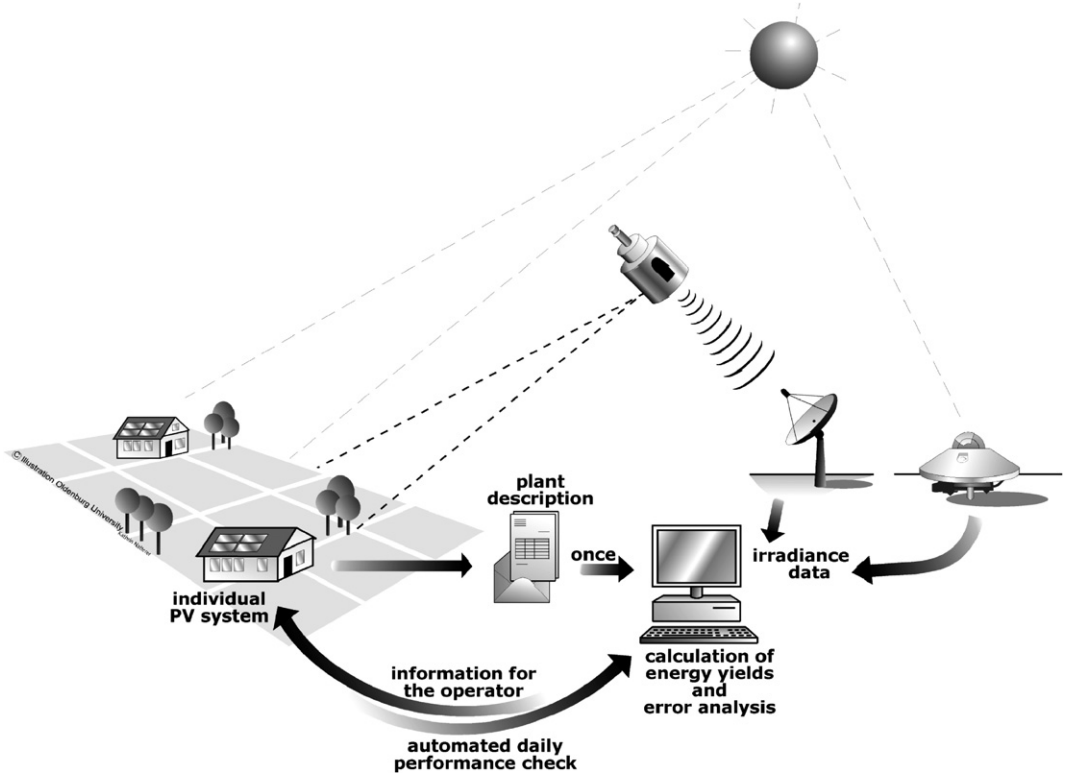

Fig. 1. PVSAT-2 overview scheme.

compared daily by the automated failure detection routine (FDR) (Stettler et al., 2005). This algorithm detects the occurrence of a malfunction and identifies typical error patterns that characterize the possible system failure (Section 4). Finally, it informs the operator about the system's performance and, in case of a malfunction, about the most likely failure sources.

The irradiance data set can be refined with hourly ground measurements from distributed weather stations by the method "kriging-of-differences" (KoD) (Betcke and Beyer, 2004). The potential of the integration of ground data has been investigated in a separate study (Section 3.1.1). KoD has not been applied in the overall routine for the test phase but will be part of the commercial service in the future.

3. Simulation of the system's energy yield

The simulation of the expected energy yield is an essential part in the PVSAT-2 service. Its quality determines the reliability of the failure detection.

Fig. 2 illustrates in a schematic overview the components as described in the methodological Sections 3 and 4. The parts of the PVSAT-2 procedure that have been in operational use during the test phase are depicted with the solid-lined elements. The expected energy yield (P_{AC}), as needed in the FDR, is derived from satellite irradiance data (G, d) as shown in the middle chain of the flow chart. The major input data to the routines are given on the left

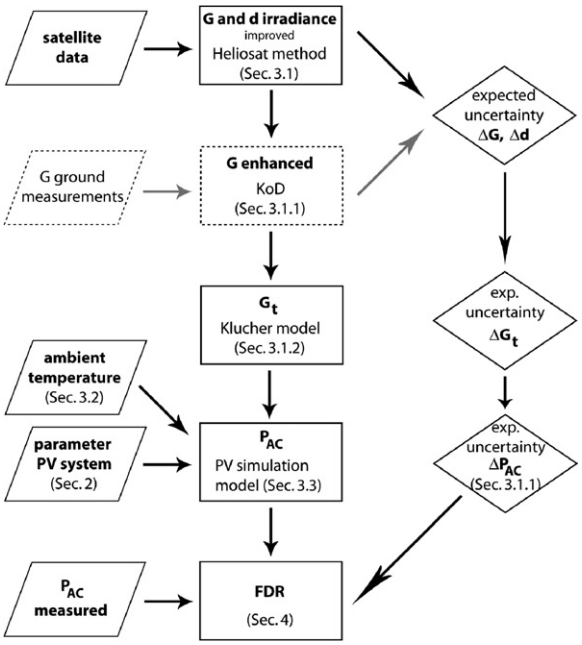

Fig. 2. Overview scheme on the applied methodology – from satellite data to a simulated PV power output for the automated FDR (Abbreviations: G, global; d, diffuse fraction; t, tilted. Symbology, rhombus – input data; squares, steps in the method; diamonds, expected maximum uncertainty of the simulation).

side. The dashed-lined elements and gray arrows explain how the results of the performed KoD study can be implemented into the processing chain. Moreover, additional

information on the accuracy on the PV simulation results (ΔP_{AC}) is prepared for further utilization in the FDR as displayed with diamonds on the right side. The corresponding sections to all elements are given in brackets.

3.1. Solar irradiance information from satellite data and ground measurements

The incoming solar irradiance is determined hourly using data from the geostationary meteorological satellite Meteosat-8. This satellite is located above the equator and near the prime meridian (3.4 °W, 0 °N). It takes images of Europe and Africa every 15 min. The spatial resolution of one Meteosat-8 pixel in the used high resolution visible channel (HRV) is 1.0×1.0 km at the sub-satellite point. In mid-European latitudes an area of approx. 1.25×1.75 km is covered. The HRV channel is sensitive in the spectral range between 0.6 and 0.9 μm (Eumetsat, 2005).

The global (G) and diffuse (D) irradiance is determined by the Heliosat method (Hammer, 2000; Hammer et al., 2003). Information on the diffuse fraction (d) and the direct beam irradiance is necessary for the conversion of the horizontal irradiance to the tilted plane.

The quality of the satellite-derived irradiance is influenced by seasonal and daily variations in sun elevation and the occurrence of cloud cover. The errors are larger for broken cloud or overcast situations than under clear sky conditions. Furthermore, systematic deviations between ground measured and satellite-derived global irradiance depending on the season are found using the Heliosat method: an overestimation during the winter time and a small underestimation in the summer months. Hence, it was necessary to improve and to enhance the method for the purpose of PVSAT-2. For the development of an adapted method, long-term time series of Meteosat-7 and shorter time series of Meteosat-8 data were available according to the operating times of the satellite. Meteosat-7 has nearly the same characteristics as Meteosat-8, but its temporal (30 min.) and spatial (4×5 km) resolution is coarser.

A variable description of cloud covered weather situations – overcast and broken cloud – to account for the different seasons and varying diurnal cloud situation has been introduced in the Heliosat method (Lorenz, 2004). A better accuracy of global irradiance could be achieved and therefore, for the diffuse irradiance as well. The quality of the diffuse irradiance is improved additionally by a spatial variability correction. The better accuracy is given in Table 1 for Meteosat-8 calculated with the enhanced Heliosat method in comparison to Meteosat-7 calculated with the enhanced and the old Heliosat method. The evaluation has been carried out for 20 meteorological stations of the German Weather Service (DWD) from April 2004 to March 2005. For Meteosat-7 data and the old Heliosat method the accuracy ranges between 5.7% for monthly and 21.8% for hourly values. A small bias of −1.5% can be observed. Within the PVSAT-2 test phase the enhanced Heliosat method on Meteosat-7 data has been used. The *rmse* between 4.7% for monthly and 20.6% for hourly values shows that the enhancements have improved the seasonal cycle of the irradiance data with a significant improvement on the monthly base. With Meteosat-8 better results were achieved on the hourly bases due to the higher temporal and spatial resolution of the satellite. Meteosat-8 will continue the service in the future.

Table 1
Overview on the accuracy of the satellite-derived irradiance data before (Meteosat-7) and after (Meteosat-7 and 8) the introduction of improvements

Error (%)	Meteosat-7 Heliosat method	Meteosat-7 enhanced Heliosat method	Meteosat-8 enhanced Heliosat method
Rmse – hourly	21.8	20.6	19.9
Rmse – daily	11.9	10.7	11.0
Rmse – monthly	5.7	4.7	5.5
Bias	−1.5	−1.8	−2.5

The quality of the irradiance data strongly influences the overall quality of the procedure. The accuracy depends on the sun elevation angle, influencing diurnal and seasonal accuracy, and the predominant weather situation, i.e., clear sky conditions or cloudy skies. The left part of Fig. 3 illustrates as an example the coincidence of satellite-derived values and ground measurements of global irradiance for a clear sky day. A confidence interval or error forecast, taken as two times the standard deviation of the errors, represents an area in which the curve of ground measurements and satellite values should agree. The right part of Fig. 3 compares both curves under conditions of variable cloud cover. The confidence interval of the satellite data is larger for cloudy sky than for clear sky conditions.

For the use in the PVSAT-2 scheme, small errors coincides with high PV power production. This means that the automatic failure detection can be fast under clear sky conditions. Less favorable conditions need averaging over longer time periods.

3.1.1. Data fusion of satellite-derived irradiance and ground measurements

It has been investigated whether further accuracy improvement of the irradiance information could be achieved by combining the results of the enhanced Heliosat method with irradiance data measured with pyranometers at meteorological stations. In earlier work (Beyer et al., 1997) encouraging results for monthly irradiation data were achieved using a "kriging-of-differences" method (KoD). For PVSAT-2, it has been investigated whether this method can also be applied to hourly data.

The method consists of three steps: first, the difference between pyranometer measurement and the Heliosat result is determined for the site of the meteorological station. This defines the necessary correction to be applied to the Heliosat results. Second, this correction is interpolated to the site of the PV system. Finally, the interpolated

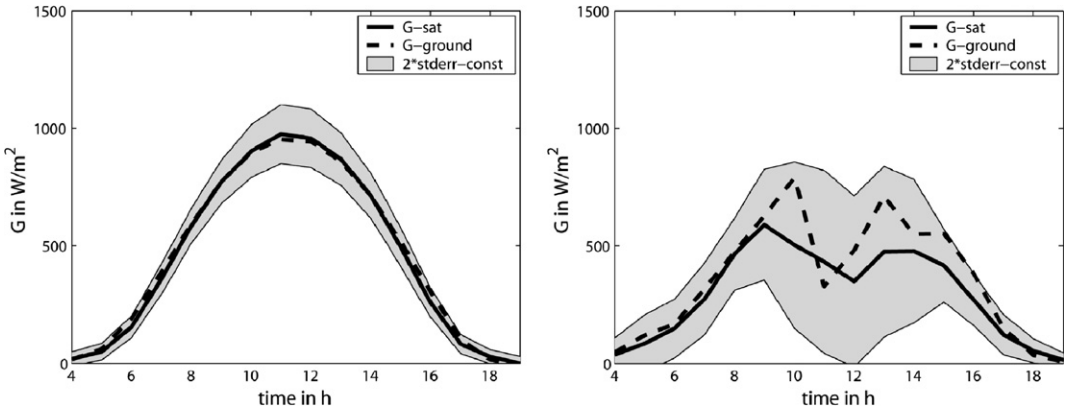

Fig. 3. Exemplary hourly error ranges for satellite-derived global irradiance compared to ground measurements under clear sky (left) and cloudy sky (right) conditions.

correction is added to the irradiance value determined with the enhanced Heliosat method at the PV system site.

As interpolation method normal kriging (see for example, Isaaks and Srivastava, 1989) has been applied for comparison.

Normal kriging takes the spatial variability of the field into account when determining the weighting factors for the interpolation. Consequently, the result is BLUE (Best Linear Unbiased Estimate), and an estimate of the uncertainty of the interpolation result is given.

The KoD method has been cross-validated on three data sets. The results are compared with the Heliosat method and interpolation of ground data with kriging in Table 2. It is evident that for the inter-station distances in these data sets the Heliosat method is considerably more accurate than straightforward interpolation of ground data. The *rmse* of KoD method is comparable with that of the Heliosat method. KoD improves the bias and the bias of standard deviation, but increases the dispersion which is the dominating factor of the *rmse*. This indicates that on an hourly time scale the deviation of the Heliosat method is dominated by an effect on a spatial scale smaller than the distance between the available meteorological stations.

Applying KoD to the entire data set is thus not necessarily useful.

However, as illustrated in Fig. 4, KoD does significantly improve the results at lower irradiance classes (0–400 W/m^2).

Furthermore, a significant decrease of the errors due to KoD is achieved under specific weather condition where cloud cover is difficult to distinguish from clear sky conditions over a snow covered surface. It therefore makes sense to use the method only selectively.

Improving the accuracy for low irradiance classes will extend the period in which significant deviations between measured and simulated yield can be detected. Selective use of the KoD method is currently investigated.

Table 2
Error measures for the three investigated methods. All measures are expressed as percentage of the average ground measured irradiance during daylight hours

Datasets	Country	Ireland	Spain	Sweden
	Nr of stations	7	30	10
	Average distance (km)	120	180	192
Heliosat	RMSE	21.0	17.5	20.6
	MBE	0.8	0.4	−1.1
	BoSD	−0.8	−1.7	−7.6
	Disp	21.0	17.4	19.1
Kriging	RMSE	33.4	32.1	38.9
	MBE	−0.2	−0.7	0.2
	BoSD	−6.8	−5.7	−9.5
	Disp	32.7	31.5	37.8
	Predicted RMSE	35.3	34.2	46.4
KoD	RMSE	22.3	17.4	21.0
	MBE	0.1	−0.1	0.1
	BoSD	0.6	−0.6	−3.3
	Disp	22.3	17.4	20.7
	Predicted RMSE	23.6	18.4	23.5

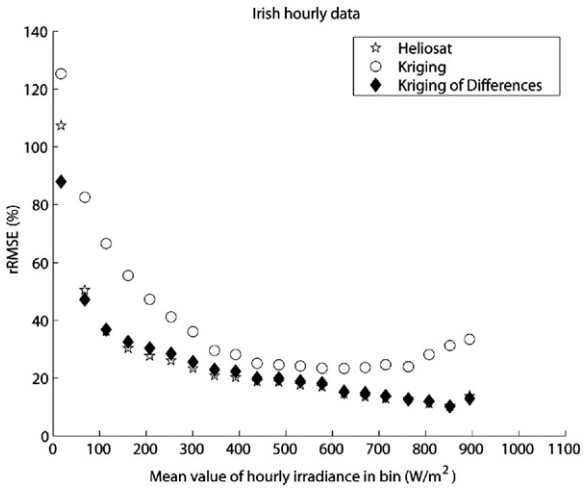

Fig. 4. The relative *rmse* of the Heliosat, kriging and kriging of differences methods for twenty irradiance classes. The results have been calculated for seven meteorological stations in Ireland with an average distance of 120 km.

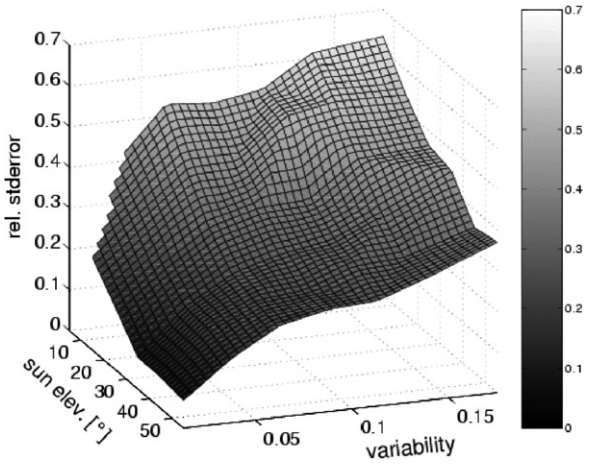

Fig. 5. Influence of sun elevation and variability on the hourly quality of satellite-derived irradiance data (Meteosat-7).

3.1.2. Conversion of horizontal irradiance to the tilted plane

The incoming irradiance is received by most PV systems on a tilted plane. The horizontally determined global irradiance has to be converted according to the installation, orientation and declination of the modules for processing in the PV simulation model. Here, the anisotropic-all-sky model formulated by Klucher (1979) is used. The Klucher model considers the diffuse sky as a superposition of an isotropic diffuse background, a circumsolar disc, and horizontal brightening.

The input data, global and diffuse irradiance, are derived from satellite data by the enhanced Heliosat method. The diffuse fraction is extracted from the global irradiance by an improved approach of Skartveit et al. (1998), (see Lorenz, 2004). The site information on the PV system such as orientation and declination are part of the information supplied by the operators of the system. Furthermore, a horizon line and the position and size of nearby obstacles like neighboring houses, trees, or roof-mounted objects can be considered.

Furthermore, diffuse and direct irradiance information is used to consider losses caused by reflectance. The direct irradiance information is used to calculate irradiation losses with a transmission function due to reflectance and transmission properties of a standard glass/EVA/coating/c-SI – surface compounds. It is a function of the sun's incident angle calculated for every hour of the day. Losses in diffuse and ground reflected irradiance are as well considered by a transmission function which is a function of the tilt angle of the PV system.

3.1.3. Accuracy information for the failure detection routine

For the use of the hourly PV simulation data in the failure detection routine, the irradiance values have to be supplied with expected, situation-specific error margins. This avoids false alarms caused by the uncertainties of the irradiance calculation that dominates the quality of the yield simulation.

The assessment of the error margins is shown in the right chain of Fig. 2 (diamonds). ΔG and Δd stand for the expected maximum deviation between ground measured and satellite-derived global irradiance G and diffuse fraction d.

The deviations are precalculated in an extensive weather-dependent error assessment for the global irradiance as well as for the diffuse fraction. Here, hourly satellite values and ground measurements were evaluated in dependence of cloud cover, variability in cloud cover, and sun elevation angle as illustrated in Fig. 5. Fig. 5 shows the standard error obtained from Meteosat-7 data in dependence of sun elevation and variability in cloud cover. The variability in cloud cover is defined as the standard deviation in cloud cover for a region of 5×3 pixel around the considered pixel. For hourly values, the error can decrease to 5% for high sun elevation angles and a low variability in cloud cover. But under a high variability in cloud cover and low sun elevation angles the error rises up to more than 40%.

As a result, typical errors (ΔG and Δd) for each possible weather situation are derived. To determine the errors for the tilted plane the Klucher model and error propagation are used in a first step. In order to validate the error forecast, the calculated expected errors are compared to a selected data base of irradiance measurements on the tilted plane (test set-up by Meteocontrol GmbH). Empirically, weights in dependence of G have been defined by fitting the approximated uncertainties to the selected data base. In the last step ΔP_{AC} is defined as $\Delta P_{AC} = 1.05 * \Delta G_t$. For properly described systems ΔP_{AC}, predicted for the PV simulation output, is dominated by ΔG_t, the uncertainty of the tilted plane irradiance. Finally, the expected errors of the energy yield (ΔP_{AC}) are used in the failure detection routine to decide whether a detected energy loss is significant.

3.2. Ambient temperature

Ambient temperature is a necessary input parameter to the PV simulation model in the PVSAT-2 procedure. It is used to calculate the PV module temperature as described in the next section. The ambient temperature is taken from the nearest weather station, typically within a radius of 30 km and a difference in height of less than 300 m, around the PV system. For Germany hourly measurements of 877 stations are available, for Switzerland 197 stations, and for The Netherlands 61 stations. In case of missing values, the next two stations in an extended radius are used.

3.3. The PV simulation model

For the simulation of the PV system's energy yield the information on the environmental conditions as irradiance and ambient temperature have to be linked to a respective system model. The model has to return the AC power fed to the grid as function of the incoming irradiance and the

ambient temperature. Within the PVSAT-2 procedure the system model is composed of the following sub-models: the DC output model, the inverter model, and a model for additional losses have to be considered.

The DC input to the inverter is modeled as the output of the PV modules at maximum power point (MPP) operation, reduced by system losses. For the MPP output a simple parametric model for the respective efficiency as function of irradiance G and device temperature $\eta_{\mathrm{MPP}}(G, T_{\mathrm{M}})$ is used. The model is based on suggestions by Randall and Jacot (2003) and is in its actual form given by Williams et al. (2003). It is composed of a characterization of the irradiance dependency of the efficiency at a device temperature of 25 °C (Eq. (1)):

$$\eta_{\mathrm{MPP}}\left(G, 25\ ^{\circ}\mathrm{C}\right) = a_1 + a_2 G + a_3 \ln\left(G \cdot \frac{m^2}{W}\right) \quad (1)$$

with a_1, a_2, a_3 as device specific parameters. The effect of temperature on the efficiency is modeled by the standard approach of a linear dependency on deviations from the standard test condition (STC) temperature of 25 °C characterized by a single temperature coefficient α.

$$\eta_{\mathrm{MPP}}(G, T) = \eta_{\mathrm{MPP}}(G, 25\ ^{\circ}\mathrm{C}) \cdot \left(01 + \alpha\left(T_M - 25\ ^{\circ}\mathrm{C}\right)\right) \quad (2)$$

The entire model uses four module specific parameters that can be determined from manufacturer's data sheets. The necessary information includes: the MPP power at standard test conditions, the MPP power for 25 °C at two irradiances different from 1000 W/m^2 (e.g., at 800 W/m^2 and 100 W/m^2) and the MPP power at 1000 W/m^2 and a temperature different from 25 °C. If data for the measured power output of systems in operation are available, the coefficients may as well be fitted to these data sets. As shown by Beyer et al. (2004) the model is applicable to modules using either crystalline silicon or thin film cell material.

To apply this model, the module temperature has to be assessed from the ambient temperature. Here, the simple assumption that the difference of module temperature T_{M} to ambient temperature T_{A} can be modeled by an offset proportional to the irradiance G is applied:

$$T_{\mathrm{M}} = T_{\mathrm{A}} + c * G \quad (3)$$

The coefficient c depends on the installation conditions (see e.g., Sauer, 1994). Table 3 shows the coefficients used for c.

The inverter efficiency to convert DC to AC is modeled by a standard approach as given by Schmidt and Sauer (1996). The model describes the efficiency as a function of the input power. Its three parameters, that may be derived from the efficiency curves, are given in the data sheets.

Table 3
Parameter c in dependence of the system's assembly

c	PV system assembly
0.058	Roof-integrated installation
0.036	On top of the roof, small roof-module distance (<10 cm)
0.027	On top of the roof, large roof-module distance (>10 cm)
0.02	Free-standing installation

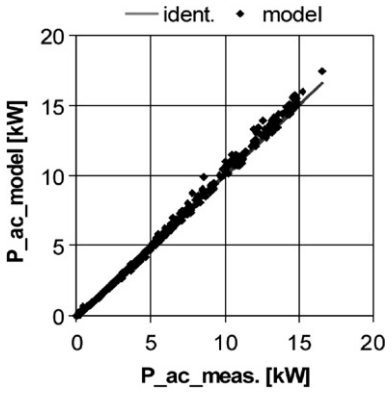

Fig. 6. Scatter plot of measured and modeled hourly power output of a 19.8 kW$_p$ PV generator, composed of five identical subsystems with 3.96 kW$_p$ (obvious erratic measurements or system malfunctions are suppressed here). This simulation is done using measured in plane irradiance and ambient temperature and the procedure as described in the text. For the data presented here (month of April), the bias of the model is <1%.

Additional system losses are separated into ohmic losses and "diffuse" losses. The ohmic losses are modeled as being proportional to the square of the DC power. If no additional information on the wiring is available the losses at nominal power are set to 2%. Under the label "diffuse" losses all losses causes by other mechanisms as mismatch due to module variability, soiling, imperfect MPP-tracking etc. are gathered. In operation, setting the "diffuse" losses to a gross value of 7% proved to be reasonable.

The model has been developed and tested independently using operational data from systems for which measured in-plane irradiance and module temperature data have been available. Fig. 6 shows an example of the model performance. Given is the comparison of measured and modeled values of the hourly averages of the AC power output of a PV generator with a peak power of 19.6 kW$_p$, composed of five subsystems with 3.96 kW$_p$ each. The data correspond to the month of April. For this month the bias of the modeled monthly energy gain is less than 1%.

4. Principles of the automated failure detection

4.1. Basic structure

The automated failure detection routine was purpose-developed for small systems owned by PV laymen who do not have the technical knowledge or do not want to be involved too much in a regular performance check of their PV system. The purpose of the routine is not only the detection of system malfunctions but also the provision of information about the most likely failure source for the client. It consists of three different parts: the failure detection system, the failure profiling method, and the footprint method. The failure detection system organizes the whole

failure detection routine. It checks the input data for consistency and availability, evaluates the results of the permanently running footprint method and decides if the second routine, the failure profiling method, needs to be started. If the monitored energy yield is significantly lower than the simulated one, as defined by confidence intervals, the two failure detection algorithms search for the most probable cause of the system's malfunction. The combined algorithm processes the recorded values of a PV system's energy production by analyzing the different aspects of the loss (Section 4.2) and applying a special statistical approach of averaging these values to reduce uncertainties (Section 4.3). The results of both routines are failure indicator levels (0–4) allocated to error probabilities for each possible failure. Finally, the failure detection system aggregates the results of both methods and the most likely failure sources are identified. The detectable system failures are given in Table 4 sorted by their general failure type.

4.2. Functionality of the failure profiling method

For the detection of systems failures, the failure profiling method is one of the applied approaches. It investigates the properties of the energy loss such as amount, duration, changes, and correlation with neighboring PV systems. In addition, it investigates ambient temperature which is delivered from a nearby weather station. The findings of this analysis are used to create a failure profile by listing the attributes of the occurred failure. This failure profile is compared to predefined failure profiles. For example, shading is indicated by a significant loss of more than 3 h a day while grid outage is defined as a total loss for a maximum of 5 h a day. Hereby, a predefined failure is excluded as being unlikely if at least one actual failure attribute is contradictory to the attributes of the predefined profile. The better the actual failure profile matches one of the predefined failure profiles, the higher is the probability that this failure has occurred. The predefined profiles were developed exploiting the characteristics of energy losses of different defects. The result of the failure profiling is an indicator level for each failure source.

Table 4
Detectable failures sources

General failure type	Failure
Constant energy loss	Degradation
	Soiling
	Module defect
	String defect
Changing energy loss	Shading
	Grid outage
	High losses at low power
	Power limitation
	MPP-tracking
	Hot inverter
	High temperature
Snow cover	Snow cover
Total blackout	Defect inverter
	Defect control devices

The failure profiling can distinguish very well between constant energy losses of some percent (degradation, soiling, string or module defect), total blackout (due to inverter defect or defect control devices) and short-time changing energy losses (shading, hot inverter, MPP-tracking etc.). Additionally, by considering the ambient temperature, it reliably excludes impossible faults, e.g., snow cover occurs only at cold winter days and the probability for malfunctions because of hot modules rises on hot summer days. The patterns for possible system faults are stored in failure categories (see Table 4). To distinguish between individual failures in one failure class is difficult because of similar failure patterns. The potential of the failure profiling to separate the individual failures in one class increases with increasing energy loss and a higher accuracy of the simulated energy yield.

4.3. Functionality of the footprint method

The second approach in failure detection is the footprint method. The footprint method aims also at the identification of minor energy losses due to shading, permanent power loss, or inverter malfunctions. To better account for the uncertainties in the irradiance calculation, a special statistical approach for averaging is applied. It analyses patterns in dependency of three different domains: normalized monitored power, time (hour of the day), and sun elevation, e.g., the influence of shading on the power production is highest at low sun elevations.

The footprint method has been developed by analyzing typical system faults in the hourly system data of well monitored PV plants within the German 1000-roofs program. The footprint method compares the pattern between measured and simulated PV power output to derive an error pattern. This error pattern is compared to typical error patterns of selected system faults in dependence of the three different domains.

Since the simulated PV power is accompanied by error ranges depending on the quality of satellite-derived irradiance data, a special statistical approach of averaging is applied to prepare the data, before the routine is started. The simulated hourly PV power output values from the yield calculation routine contain errors which are mainly caused by the uncertainties of the satellite-derived irradiance. The errors can be large for individual irradiance values as shown in Section 3.1. Therefore, a basic approach in the footprint method is not to follow the time pattern of individual values, but the pattern of sample averages. The error of the sample average decreases considerably compared to the errors of individual values. Samples with different domains are defined to increase the prediction quality of the footprint method. The intention is to find samples of measured values with individual errors but having nearly the same expectation values. Within these

samples, an appropriate statistical method is applied. The samples will contain the hourly values of simulated PV power P_{sim_h}, normalised by the corresponding hourly values of monitored power P_{mon_h}, thus P_{sim_h}/P_{mon_h}. The samples in the footprint method are created by means of intervals in three different domains (see Fig. 7):

- domain of normalised simulated power P_{sim_h}/P_{inst} (capacity domain) with P_{inst} as nominal installed power of the PV system. In this domain, the hourly values of P_{sim_h}/P_{mon_h} are segmented into intervals of P_{sim_h}/P_{inst} with a step width of 0.1;
- domain of time t. In this domain, the hourly values of P_{sim_h}/P_{mon_h} are segmented into the respective hourly intervals of the day;
- domain of elevation angle of the sun *elevation*. In this domain, the hourly values of P_{sim_h}/P_{mon_h} are segmented into the respective elevation angle in steps of 5°. To detect sun elevation related effects, the day is divided into two half days around noon, and the events in identical elevation intervals are identified separately for the morning and evening.

Fig. 7 shows how the normalized hourly PV power output P_{sim_h}/P_{mon_h} are sorted into the three different domains. The values P_x denote individual values of P_{sim_h}/P_{mon_h} in this sample, whereas P^* denotes the special weighted sample average. The error bars of P^* are decreasing compared to the errors of P_x.

The sample averages P^* are calculated for three different periods of simulated and monitored data: a period of one day, a period of 7 days and a period of 30 days. For each period, sample averages will be produced in the three domains. For clear sky conditions with low uncertainties, failures can be identified on a 1-day scale. For less favorable conditions the failure identification will need a longer period of time and ΔP_{AC} is decreasing with the length of the averaged period. The sample average is given an expected error calculated from the errors of the simulated individual values in the sample.

For each interval i in all three domains, an error mark error_i^* is set:

$$\text{error}_i^* = \begin{cases} 1 & \text{for } (P_i^* - 2S_i^*) > 1.0; \\ -1 & \text{for } (P_i^* + 2S_i^*) < 1.0; \\ 0 & \text{else} \end{cases}$$

with s_i^* as standard deviation of the error. Weather situation-specific errors are assumed to be Gaussian distributed, a factor 2 is applied in order to cover 95% of the sample values.

Consequently, the meaning of the error mark is:

- $\text{error}_i^* = 1$ simulated power production is significantly larger than than monitored;
- $\text{error}_i^* = -1$ simulated power production is significantly less than monitored;
- $\text{error}_i^* = 0$ monitored power production is within the error range of simulated power production.

For the extraction of an error pattern shading is tracked as an example failure throughout the next paragraphs, displayed in Figs. 8 and 9.

Fig. 8 illustrates the distribution of P^* values in the different domains. The definition of the error marks allows to extract an error pattern from this set of P^* sample averages. This error pattern is shown in Fig. 9, constructed by replacing the P^* values by the corresponding error_i^* values in both domains. With this approach, the performance of the PV system in the considered 1-day, 7-day, or 30-days period is expressed by a simple error pattern distribution in the domains.

The extracted error pattern is then compared to predefined error patterns for a set of typical PV system faults or power limiting operation modes. The pattern shown in Fig. 9 is similar to a shading pattern caused by a low far horizon. Consequently, the power loss occurs mainly at low values in the capacity domain, in the morning and evening hours in the time domain, and in the low elevation intervals of the elevation domain.

As a result of the comparison, the probability value for a certain error is returned as an indicator level to the failure detection system. The probability values are determined by distributing weights for each mark of the error patterns. The weights naturally sum up to one for the predicted

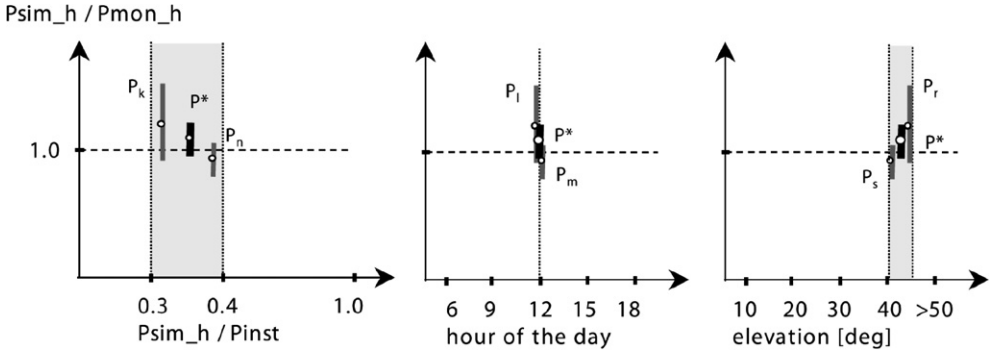

Fig. 7. The normalized hourly PV power are sorted in the three domains: capacity domain (left), time domain (middle), and sun elevation (right).

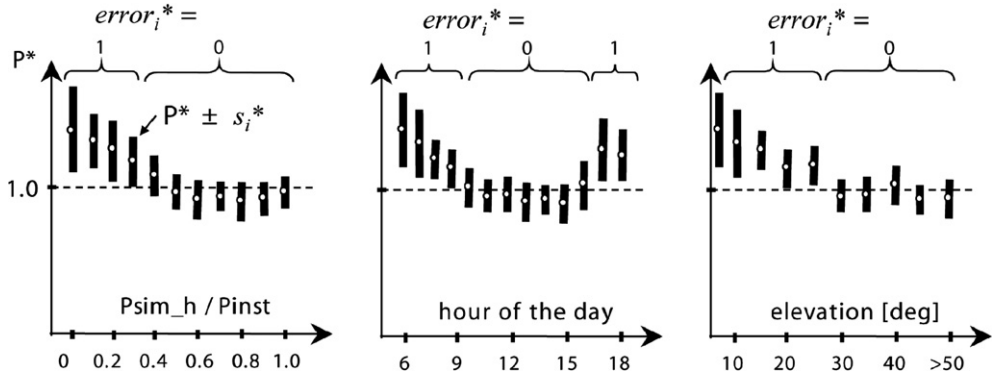

Fig. 8. Sample averages P^* with error bars in the three domains: capacity domain (left), time domain (middle), and sun elevation (right).

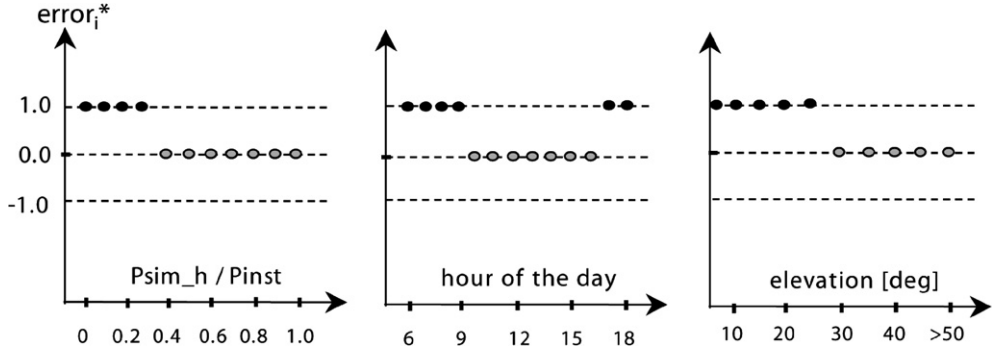

Fig. 9. Extracted error pattern for shading displaying the values of the error marks in the three domains: capacity domain (left), time domain (middle), and sun elevation (right).

patterns in each domain. If an error mark matches a predefined error mark, the weights of the corresponding marks are summed in each domain to determine the probability of the occurrence of a specific error. Finally, the probabilities of each domain are multiplied for the specified system failures. According to threshold values the total probabilities for all failures are examined. If a probability is larger than 0.9, the occurrence of the detected fault is very likely, while a value lower than 0.6 indicates an unlikely failure source.

5. Application in the field test

5.1. Introduction

In the test phase, the performance of 100 PV systems in three European countries was monitored daily between February and September 2005. Before that, the PVSAT-2 procedures were tested with historic data of 21 well-described PV systems. The effectiveness of the entire PVSAT-2 routine as described in this paper was thoroughly checked to identify application limitations. Corrections and improvements of discovered bottlenecks have been introduced right away.

Fig. 10 shows the geographical and size distribution of the analysed PV systems of the test phase. In total 36 Swiss, 34 German, and 30 Dutch systems were evaluated. The distribution of rated power of the systems is shown in Fig. 11. Difference in the size of the systems can be observed between the countries. In the Netherlands 57% of the systems were smaller than 1 kW_p; the average rated power was 1.3 kW_p. In Switzerland 50% of the systems were between 3 and 4 kW_p, with an average rated power of 7.3 kW_p. In Germany, the sample systems showed a large variety in size with an average of 4.7 kW_p. Overall the range of tested system sizes has been very wide. Also the diversity in module and inverter types was very high; 57 different module types and 38 different inverter types were present in the test phase.

The owners of the PV systems provided the information that was required for the energy yield simulation for the field test; e.g., the system configuration, the number and type of modules and inverters, the orientation, tilt and mounting type and the year of installation. During the field test the local data loggers sent the 15-min or sometimes hourly energy yields from the involved systems to a central server.

Also irradiance values were available from either a pyranometer or from reference cells for the part of the test phase where historic data were used. Therefore, also the quality of the satellite-derived irradiance values could be evaluated. During the test phase Meteosat-7 data and the enhanced Heliosat method has been used.

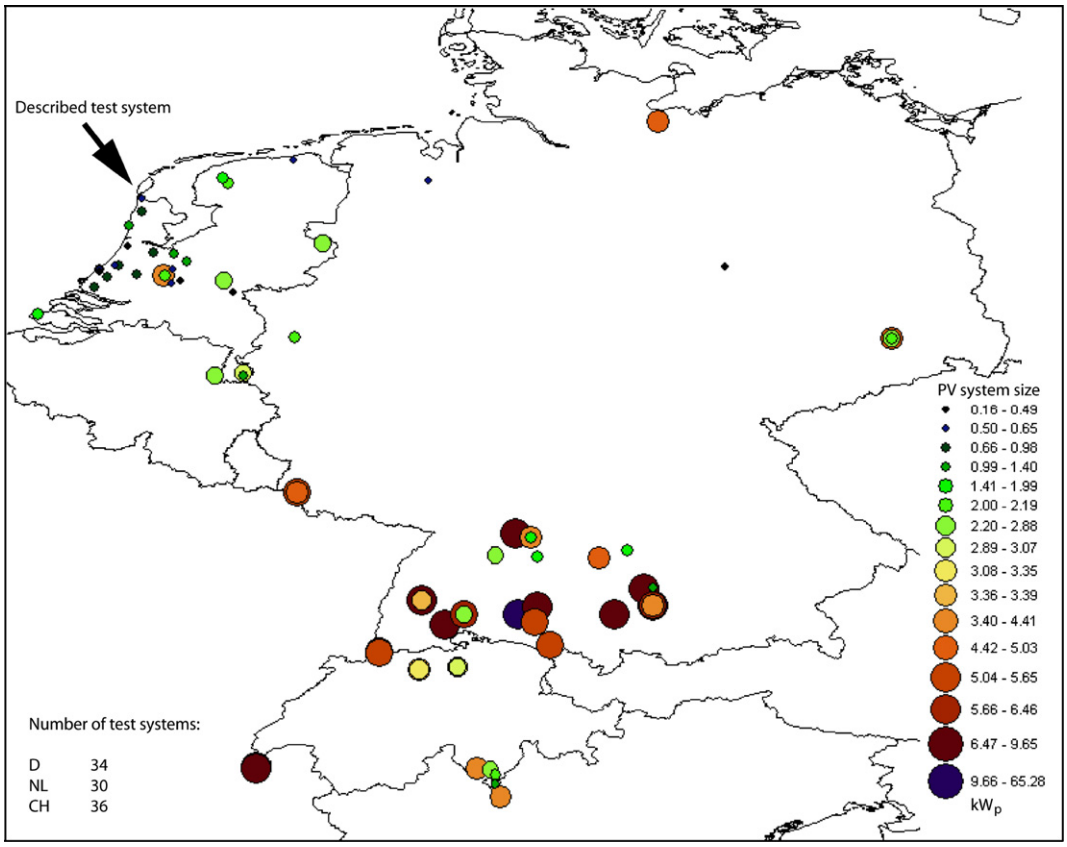

Fig. 10. Geographical distribution and size of the PV systems in the PVSAT-2 test phase.

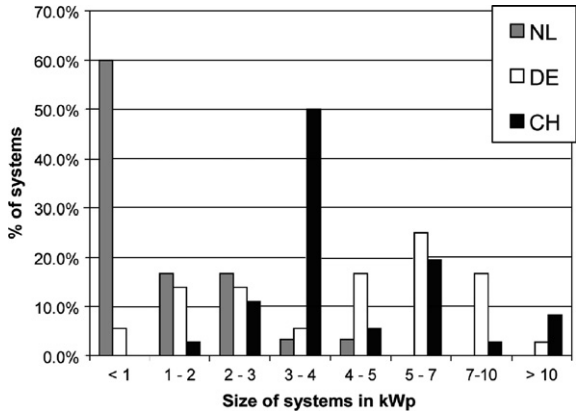

Fig. 11. Distributed power rating of the PV systems participating in the test phase.

5.2. Performance of the energy yield simulation

The quality of the satellite based irradiance calculations was analysed by comparing measured irradiance values to simulated ones for the 21 systems in the historic test phase. For every month and for the total year, the bias, hourly and daily *rmse*, and the reliability of the error expectation were calculated. The yearly bias was between −5 and +8% for the different systems. Here, it should be kept in mind that often reference cells were used for the measurements of the irradiance. The relative average hourly *rmse* was between 26 and 34% for systems with a smaller tilt angle (<40°). The relative average daily *rmse* ranged between 12 and 16% for these systems. The reliability of the error forecast is measured by the percentage of hourly measurement values that are within the simulated value plus or minus the expected maximum uncertainty of the error. The error forecast might be slightly conservative; between 97 and 99% of data were in this interval. This means that although the irradiance calculation does not have the high accuracy of ground measurements, the predicted error forecast is more than sufficient to cover this uncertainty.

For the majority of well working systems in the historic test phase the quality of energy simulation was high. For several other systems, the real peak power of the modules seemed to deviate from the data sheet information. This was minimal for several systems of which the flash test power was used.

During the field test problems were encountered with the simulated energy yields. For 52% of the test systems the simulation was fine and a discrepancy with the measurements could be explained by failures. For 48 systems the uncertainty of the simulation was larger than expected. This was partly caused by incorrectly described systems in the registration form filled in by the owner of the PV system. For 25 systems, the azimuth angle was not correctly specified in the registration form. This strongly influences

the hourly simulated energy yield, and, if not corrected, can result in an indication for shading. This can easily be identified on a daily comparison basis. As an example, Fig. 12 shows a 416 W_p system with four modules from Den Haag, The Netherlands with a user-specified azimuth of 180°. The original simulated energy yield is shown by the dotted line; from the measured energy yield (solid line), it is clear that the system is in reality oriented more towards the east. It was derived that the real azimuth should be 155°. This was later confirmed by the owner of the system. The change in the azimuth angle in the system description resulted in a high quality simulation of the energy yield. In Fig. 13 the hourly measured and simulated energy yield are shown versus the irradiation values. The performance ratio (PR) for this system was 0.80. As expected the quality of the simulation was higher in June than in February. The bias for this system in the period from 15th February to 20th June was −3.2%. The monthly values ranged from −1.5% in May to −5.8% in February. The relative hourly and daily *rmse* for this period were, respectively, 18.5 and 9.8%. The hourly *rmse* ranged from 13.3% in May to 29.9% in February. Ninety-seven percent of the measurement values were within the range of the simulated value plus and minus the expected maximum uncertainty.

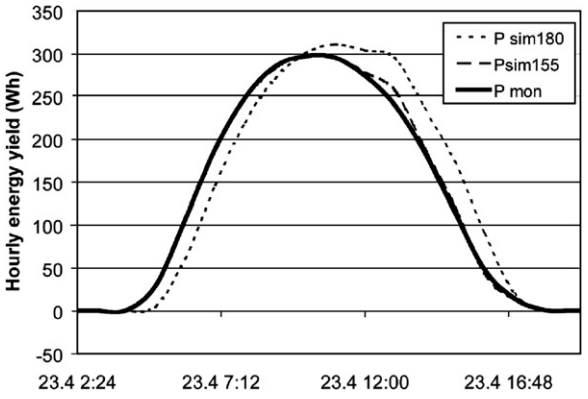

Fig. 12. Simulated energy yields after a wrong specification of an azimuth of 180°. It could be corrected to the right value of 155°.

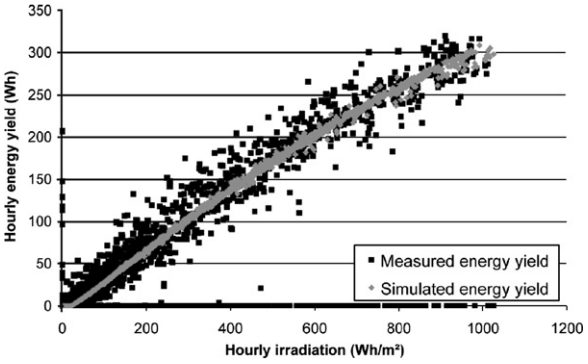

Fig. 13. Improved simulation quality after the correction of the azimuth.

Other causes for a deviating simulation were, e.g., a wrongly specified mounting type and more than average cabling losses (Prignitz, 2005). If the mounting type is specified as 'small module-roof distance' instead of 'roof integrated', this can easily result in an overestimation of ca. 7% for a nice day. Partly the problems are also caused by deviations from data sheet information of the specified modules and inverters. Besides the tolerance of 5 or 10% of the peak power stated in the data sheets, also aging of the modules can result in an efficiency loss. For the correctly described system the simulation was dominated only by the uncertainties of the irradiance. Under field test conditions it turned out that incorrect system description is a problem.

The above information suggests that a one month learning phase is needed to eliminate all false specifications from the PV system description. Especially, if registration forms are filled in by laymen slightly wrong specifications cannot always be prevented. If the technical functioning is known to be correct, the simulation model parameters could automatically be adjusted (Prignitz et al., 2006).

5.3. Performance of the automated failure detection routine

The automated failure detection routine as described in Section 4 was tested with historic data and in the field test. The historic data included data from well-described systems with failures. This was used to test, and where necessary adapt and improve, the failure detection routine. Failures in the field test occurred in an uncontrolled environment: no artificial failures were generated. Several types of failures that occurred and have been detected are described in the following sections.

5.3.1. Example system with a string error

In this section, one example system is described in detail to explain the functioning of the failure detection routines. This test system will be followed throughout the test phase. The PV system has been installed in 2000 in Den Helder, The Netherlands (see Fig. 10). It consists of six Shell 95 RSM AC modules and six NKF OK-4 inverters with a total rated power of 570 W_p. The orientation is exactly south (180°) with a tilt angle of 40°. The data logger was installed on February 18th, 2005 to monitor the performance of the system.

Fig. 14 shows the monitored (P_{mon}) and the simulated (P_{sim}) power output of the system for different time spans. In Fig. 14a both lines are close together within the ranges of the error bars around the simulated energy yields. This shows that the system was operating correctly in the early stages of the test phase. In Fig. 14b it is shown that after the 30th of March a persistent difference between the measured and simulated energy yield occured. This might indicate a failure. Direct feedback from the operator revealed that one out of six inverters had broken down. This loss is not significant on an hourly basis; a failure was not detected continuously. Fig. 15 shows the hourly measured

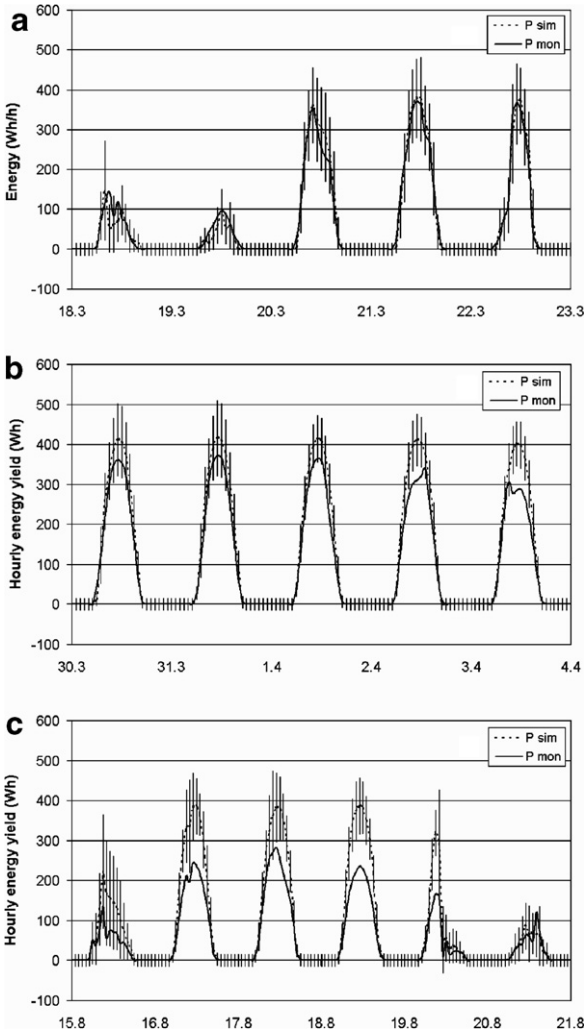

Fig. 14. Simulated and actual energy yield curves of the example system in Den Helder. (a) Error-free running system; (b) breakdown of one inverter; (c) after the breakdown of the second inverter.

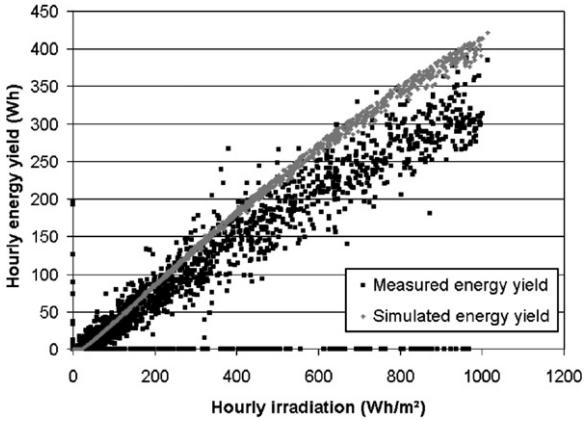

Fig. 15. Simulated and measured energy yields over satellite-derived irradiance for the period with one broken inverter.

and simulated energy yield versus the simulated irradiation for the period with one broken inverter. Especially, under high irradiances large deviations can be observed. In the second week of August, a second inverter broke down. In Fig 14c it can be seen that hourly energy losses for nice weather days, nearly clear sky conditions, are much larger than the error bars. This is not true for days with cloudy skies like the 15th of August. After detection of a permanent power loss for two defect strings by the footprint algorithm, the failure was confirmed by the test user. The exact time when the inverter broke down is not known. It took about 10 days to identify the failure due to cloudy conditions.

The defect of one of the six inverters had caused a 17% energy loss. For the majority of the days, this is too low to be detected by the failure profiling method, due to the uncertainty in the daily energy yield simulation. Initially, also the footprint algorithm did not detect a permanent power loss in April.

In Fig. 16 the footprint scheme of a power class analysis at four different days of a 30-days averaging period is shown. In the integrated table the error_i^* -values for the different days are presented. For the 25th of March, the measurement points of this day plus the previous 29 days are distributed over the intervals (based on simulated power divided by the installed power). On the 25th of March there is no error indication ($\text{error}_i^* = 0$) for any interval, as expected since there is no failure. On the 25th of May there is an error indication ($\text{error}_i^* = 1$) for three intervals. The occurrence of a fault has been detected but up to now the failure source could not be identified. At the lower power ranges the uncertainty is still too high to detect the failure permanent power loss. On the 25th of July, there is a failure indication for the majority of the intervals. For the 25th of September with two out of six inverters defect, the footprint algorithm has a failure indication for almost all intervals. A final failure indication of the footprint algorithm results after weighting of the individual failure indications. For a permanent power loss an error in all intervals is expected for both the power class domain and the time domain. For the days in July and September this resulted in a failure indication for permanent power loss. Basically from half June onwards the footprint algorithm detects permanent power loss for almost every day on a 30-day analysis. On nice weather days permanent power loss is also detected for a 7-day and a 1-day period.

The failure profiling method detects a failure if the daily energy loss is larger than two times the standard error of the daily energy yield. In Fig. 17, the minimum daily energy loss for detection by the failure profiling method (in percentage of simulated energy yield) is given versus the daily irradiation for this system. The solid line indicates an energy loss of 16.7% corresponding to one defect inverter out of six. It shows that only on very nice days ($> \sim 7000\ \text{Wh/m}^2$) an energy loss will be detected. The dashed line corresponds to an energy loss of 33% or two broken inverters. It can be seen that this is detected as well on days with very reasonable weather ($> \sim 3000\ \text{Wh/m}^2$).

As expected the failure profiling method detects a significant energy loss on several days. It classifies the energy loss

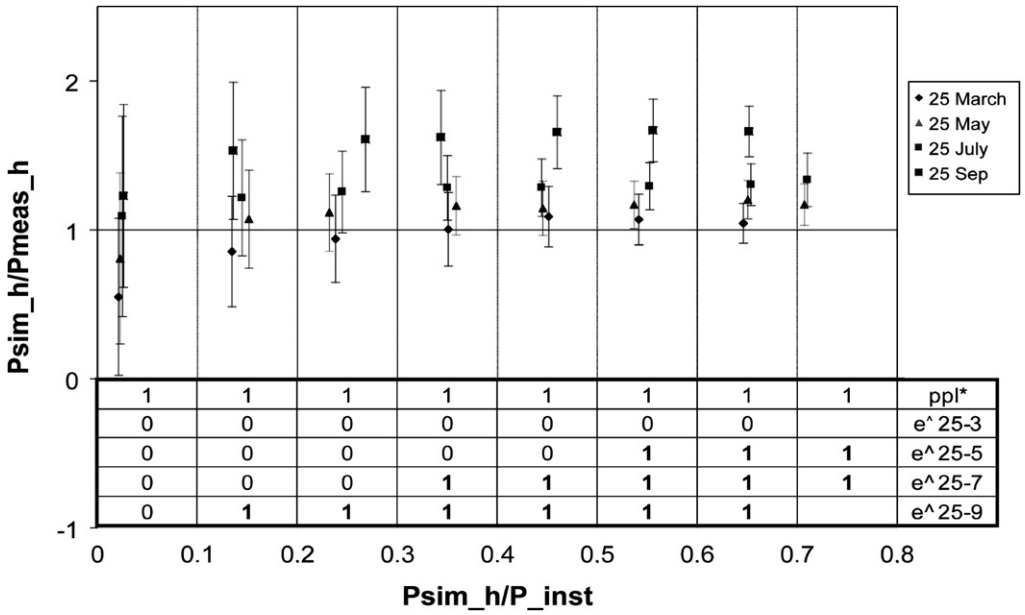

Fig. 16. Footprint scheme in the capacity domain for a 30-days period of investigation. A first error indication appears on the 25th May, 2005 (ppl* = failure pattern for permanent power limitation; $e^{\wedge}$ = errori* for a 30-day period up to the specified date (day-month)).

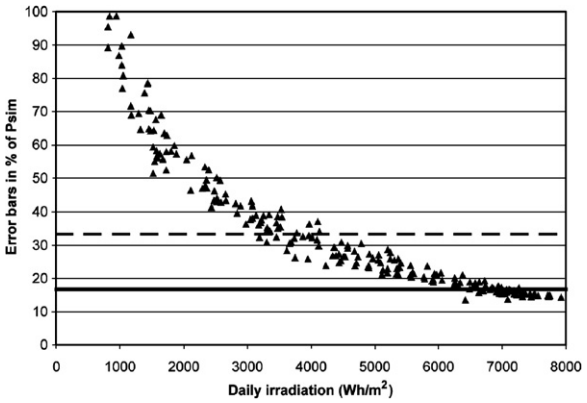

Fig. 17. Minimum required energy loss for daily values for a reliable detection of the example inverter failure.

into different failure type categories. The main difference relevant in this case is that it can be defined as constant or changing energy loss. A defect inverter is a constant energy loss, but for example shading is changing throughout the day. The results of the entire failure detection routines are shown in Fig. 18. A bubble indicates the detection of a failure; the size of the bubble indicates the possibility that the energy loss is caused by this failure. On the days that a total blackout was detected the data logger did not send data to the server or it was disconnected from the telephone line. The detected failures on the other days are caused by the defect inverter(s). The footprint algorithm detects a permanent power loss on a regular basis from half June onwards. The failure profiling method mostly succeeds on nice days to identify a constant energy loss. Sometimes also changing energy loss is given as an explanation for the energy loss.

5.3.2. Further example failures

This section gives a short overview on some more failures that have been successfully detected during the test phase.

5.3.3. Shading

Both the failure profiling method and the footprint algorithm have a detection routine for shading. The footprint identifies shading at low sun elevations, so early in the

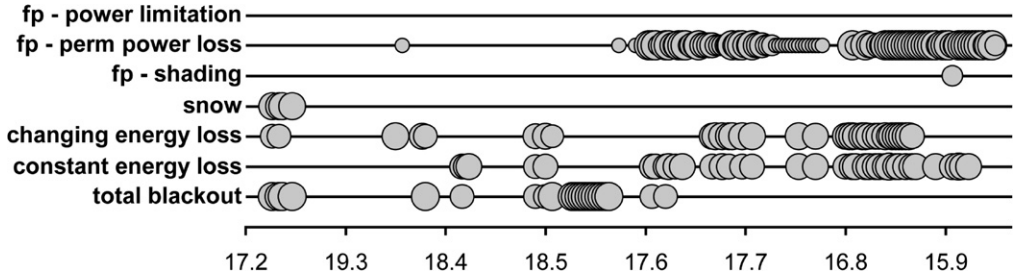

Fig. 18. FDR results. fp, failure soure indication by the footprint method; others, results of the failure profiling method.

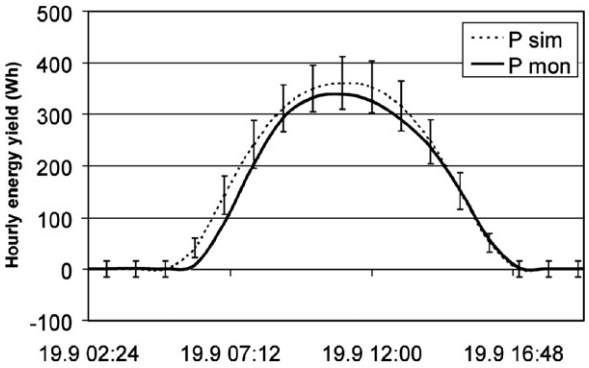

Fig. 19. Shading example at a Dutch system.

morning or late in the afternoon. The shading area is largest when the sun is low. An example for a day when the footprint detects shading is given in Fig. 19. In this example, the shading in the morning is caused by a solar collector and a chimney. This type of shading is not detected by the failure profiling method, since the daily energy loss is not significant.

The failure profiling method detects shading if there is a significant energy loss for more than three hours a day. This is shown for one of the German systems in the test phase in Fig. 20. The shading is caused by a large tree in the garden of the owner. The footprint does not detect this type of shading since the energy loss also occurs at hours with high sun elevations.

5.3.4. Snow

Snow was detected on various occasions. An example of a system with snow is shown in Fig. 21. Low temperature and the large difference between measured and simulated energy yield indicate snow. Snow is well detected if the daily irradiation is larger than 1000 Wh/m^2.

5.3.5. Power limitation

One of the Swiss systems in the test phase has an undersized inverter. Therefore, at hours with a high irradiation an energy loss occurs. This is detected by the footprint algorithm, which studies the measured power normalised by the simulated power versus the simulated divided by the installed power. It notices that at high $P_{\mathrm{sim}\_h}/P_{\mathrm{mon}\_h}$ power intervals there occurs an energy loss. This results in a failure indication for power limitation.

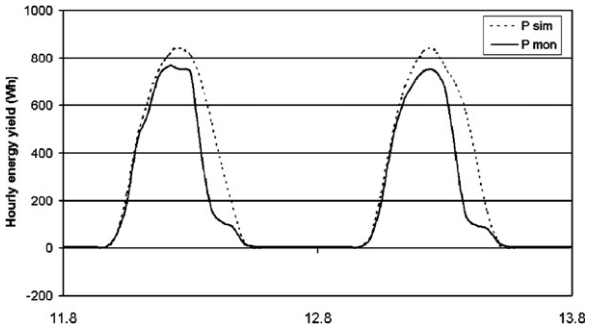

Fig. 20. Major shading at a German system.

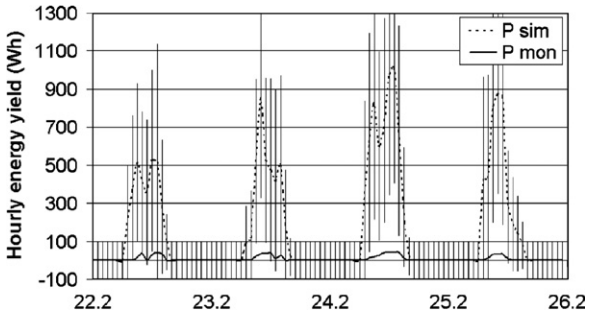

Fig. 21. Snow cover at a Swiss system.

5.3.6. Total blackout

Total blackouts are recognised on days with an irradiation of more than 1000 Wh/m^2.

More failure types were detected. It turned out that it is difficult to distinguish failure types within the category constant or changing energy loss with the failure profiling.

5.4. Summary of the test phase results

The PVSAT-2 routine was successfully tested in the field test. The automated performance check is often successful in detecting failures and identifying their possible causes. Some critical issues for the performance of the routine remain. The first is a correct description of the PV system as described in Section 5.2; this involves both the user of the service who has to correctly fill in the forms and the quality of the data sheets. If this is correct, the quality of the simulated energy yield is high as well as the quality of forecasted error margins. The introduction of an initial learning phase could solve these problems, but this would also increase the costs of the commercial service.

Second, the size of the error bars caused by the uncertainty of the satellite derived irradiance values prevent the detection of a small energy loss, e.g., a string error of 17% will only be identified in summer. Snow in March 2005 in The Netherlands was for most of the test systems not detected, because the daily irradiation was lower than 1000 Wh/m^2. If the irradiation is higher than this value, snow usually will be detected as we have seen for the Swiss system in Section 5.3.2. If the daily irradiation is high enough and the energy loss is large enough failures will be detected in a very short time. For example, if a string error causes an energy loss which is larger than 33% the chance is very high that it will be detected on days with an irradiation of more than 3000 Wh/m^2. The footprint algorithm also analyses a 30-day period and therefore also succeeds in detecting smaller energy losses. This does take a bit more time though. Also morning and evening low elevation shading is well detected.

If a defect in a system occurs, most energy is lost on days with high irradiation values. At these days, the failure

detection routine works better. The examples have shown that large enough failures can be detected fast under high irradiances.

6. Conclusion

A remote performance check including an automated failure detection routine for PV systems has been developed within the PVSAT-2 project. The procedure is based on satellite-derived irradiation data which is used to simulate the energy yield of a PV system. Improvements on the quality of the satellite-derived irradiance information have been achieved. A PV simulation model using data sheet information only suitable for modules of crystalline silicon or thin film cell material has been developed. The developed automated failure detection routine detects the occurrence of a failure and identifies the most probable cause within a time span of a few days under good weather conditions. A field test with 100 PV systems has demonstrated the benefits and present limitations of the procedure.

The accuracy of the irradiation data determines the overall accuracy of the whole procedure. The study on the assembly of an irradiance data set by combining satellite-derived values and ground measurements by kriging-of-differences has shown the potential to further improve the quality of the data. Especially under weather situations as overcast, broken cloud situations, and low sun elevations, the accuracy of the global irradiance increases. Nevertheless, the PVSAT-2 scheme has shown already a good performance in case only satellite data are available.

The simulation of the expected energy yield revealed that an exact technical description and characterization of the PV system is necessary to achieve reliable results and therefore, a reliable output from the failure detection routine. Investigations have shown that erroneous described PV systems might be corrected in an initial phase of one month. The economic value of an initial phase that requires personal attention in the commercial application of the PVSAT-2 routine still has to be determined.

The automated failure detection routine, consisting of the failure profiling and the footprint algorithm, has been adapted in the tests using historical data of well-monitored PV systems. It has shown its potential in the field test where further optimizations took place. The occurrence of system failures could be detected in a short time while the identification of the failure source took more time in dependence of the predominant weather conditions. In the process of narrowing down to the most likely failure sources, the detected system malfunctions have been sorted into different failure categories. The footprint algorithm has shown its high potential in identifying reliably the most likely failure sources.

As a result, it can be clearly stated that the PVSAT-2 routine assures economic benefits and prevents from energy losses, not only valuable in countries with a granted feed-in tariff. It helps to integrate PV as a reliable energy source into the growing mix of renewable energies supplying the energy of our future.

The PVSAT-2 procedure will be commercially offered starting in 2006 under the product name SPYCE (www.spyce.de) by Enecolo AG, Switzerland and by Meteocontrol GmbH, Germany (www.meteocontrol.de) under the designation safer'Sun Satellite.

Acknowledgements

This research was funded by Contract No.: ENK5-CT-2002-00631 from the European Union (EU). We thank the Heliosat-3 project team (Contract No.: NNK5-CT-2000-00322 funded by the EU) for their fruitful discussions on the improved irradiance calculation scheme. We are also grateful to the DWD for the provision of the ground measured irradiance data. Special thanks goes out to our test users who contributed with their voluntarily participation to the success of the project!

References

Betcke, J., Beyer, H.G., 2004. Accuracy improvement of irradiation data by combining ground and satellite measurements. In: Proceedings of the EUROSUN (ISES Europe Solar Congress), Freiburg, Germany 3, pp. 764–770.

Beyer, H.G., Czeplak, G., Terzenbach, U., Wald, L., 1997. Assessment of the method used to construct clearness index maps for the new European solar radiation atlas (ESRA). Solar Energy 61, 389–397.

Beyer, H.G., Lorenz, E., Betcke, J., Drews, A., Heinemann, D., Heilscher, G., Bofinger, S., 2004. Identification of a general model for the MPP performance of PV-modules for the application in a procedure for the performance check of grid connected systems. In: 19th European Photovoltaic Solar Energy Conference, Paris, France.

EEG, 2004. Gesetz für den Vorrang Erneuerbarer Energien. <http://bundesrecht.juris.de/bundesrecht/leeg_2004/gesamt.pdf/> (accessed February 1st, 2006).

Eumetsat, 2005. What we do – Satellites. <http:www.eumetsat.int/Home/Main/What_We_Do/Satellites/index.htm?l=en> (accessed December 16th, 2005).

EurObserv'ER, 2005. Photovoltaic Energy Barometer 2005. Systèmes solaires 166, <http://www.epia.org/03DataFigures/barometer/Barometer_2005_full_version.pdf/> (accessed February 1st, 2006).

Hammer, A., 2000. Anwendungsspezifische Solarstrahlungsinformationen aus Meteosat-Daten. Ph.D. Thesis, University of Oldenburg, available under <http://docserver.bis.uni-oldenburg.de/publikationen/dissertation/2001/hamanw00/hamanw00.html/> (in German).

Hammer, A., Heinemann, D., Hoyer, C., Kuhlemann, R., Lorenz, E., Mueller, R.W., Beyer, H.G., 2003. Solar energy assessment using remote sensing technologies. Remote Sensing of the Environment 86, 423–432.

Isaaks, E.H., Srivastava, R.M., 1989. An introduction to applied geostatistics. Oxford University Press, New York.

Klucher, T.M., 1979. Evaluation of models to predict insolation on tilted surfaces. Solar Energy 23, 111–114.

Lorenz, E., 2004. Improved diffuse radiation model. Project Report PVSAT-2. Oldenburg University (to be published).

Prignitz, O., 2005. Begleitung der Testphase des Projekts PVSAT-2 – Exemplarische Analyse der Verwendbarkeit von Datenblattangaben und Kennlinien nach Herstellerangaben zur laufenden Ertragsberechnung von Photovoltaikanlagen. Diploma Thesis, HS Magdeburg-Stendal, Germany (in German).

Prignitz, O., Beyer, H.G., de Keizer, C., van Sark, W.G.J.H.M., 2006. Vom Datenblatt zum Systemertrag – zur realistischen Modellierung

kleiner netzgekoppelten PV-Systemen. In: Proceedings of the 21st Symp. Photovoltaische Solarenergie, Bad Staffelstein, Germany.

Randall, J.F., Jacot, J., 2003. Is AM 1.5 applicable in practice? – Modeling eight photovoltaic materials with respect to light intensity and two spectra. Renewable Energy 28, 1851–1864.

RD, 2004. Real Decreto 436/2004. <http://noticias.juridicas.com/base_datos/Admin/rd436-2004.html/> (accessed February 1st, 2006).

Sauer, D.U., 1994. Untersuchungen zum Einsatz und Entwicklung von Simulationsmodellen für die Auslegung von Photovoltaik-Systemen. Diploma Thesis, TH Darmstadt, Germany (in German).

Schmidt, H., Sauer, D.U., 1996. Wechselrichter-Wirkungsgrade. Sonnenenergie 4, 43–47, in German.

Skartveit, A., Olseth, J.A., Tuft, M.E., 1998. An hourly diffuse fraction model with correction for variability and surface albedo. Solar Energy 63, 173–183.

Stettler, S., Toggweiler, P., Wiemken, E., Heydenreich, W., de Keizer, A.C., van Sark, W.G.J.H.M., Feige, S., Schneider, M., Heilscher, G., Lorenz, E., Drews, A., Heinemann, D., Beyer, H.G., 2005. Failure detection routine for grid-connected PV systems as part of the PVSAT-2 project. In: Proceedings of the 20th European Photovoltaic Solar Energy Conference & Exhibition, Barcelona, Spain, pp. 2490–2493.

Williams, S.R., Betts, T.R., Helf, T., Gottschalg, R., Beyer, H.G., Infield, D.G., 2003. Modeling long-term module performance based on realistic reporting conditions with consideration to spectral effects. In: Proceedings of the 3rd World Conference on Photovoltaic Energy Conversion, Osaka, Japan.